Imaging the photodissociation dynamics of the methyl radical from the 3s and 3pz Rydberg states

Sonia Marggi Poullain,[a] David V. Chicharro,[a] Alexandre Zanchet,[b] Marta G. González,[a] Luis Rubio-Lago,[a] María L. Senent,[c] Alberto García-Vela[b] and Luis Bañares[a]

a. Departamento de Química Física I , Facultad de Ciencias Químicas, Universidad Complutense de Madrid (Unidad Asociada I+D+i CSIC), 28040 Madrid (Spain). E- mail: lbanares@ucm.es
b. Instituto de Física Fundamental, CSIC, C/ Serrano, 123, 28006 Madrid (Spain)
c. Departamento de Química y Física Teóricas, Instituto de Estructura de la Materia, CSIC, C/ Serrano, 121, 28006 Madrid (Spain)

The photodissociation dynamics of the methyl radical from the 3s and 3pz Rydberg states have been studied using velocity map and slice ion imaging in combination with pump-probe nanosecond laser pulses. The reported translational energy and angular distributions of the H(2S) photofragment detected by (2+1) REMPI highlight different dissociation mechanisms for the 3s and 3pz Rydberg states. A narrow peak in the translational energy distribution and an anisotropic angular distribution characterizes the fast 3s photodissociation, while for the 3pz state Boltzmann-type translational energy and isotropic angular distributions are found. High level ab initio calculations have been performed in order to elucidate the photodissociation mechanisms from the two Rydberg states and to rationalize the experimental results. The calculated potential energy curves highlight a typical predissociation mechanism for the 3s state, characterized by the coupling between the 3s Rydberg state and a valence repulsive state. On the other hand, the photodissociation on the 3pz state is initiated by a predissociation process due to the coupling between the 3pz Rydberg state and a valence repulsive state and constrained, later on, by two conical intersections that allow the system to relax to lower electronic states. Such mechanism opens different reaction pathways leading to CH2 photofragments in different electronic states and inducing a transfer of energy between translational and internal modes.

Introduction

The methyl radical is of great importance due to its relevant role in different areas such as atmospheric1 and interstellar chemistry2 or hydrocarbon combustion3. Historically, as the simplest alkyl radical, it has been considered a benchmark system in molecular orbital theory for the photochemistry of large open-shell hydrocarbons.

Herzberg and Shoosmith4 reported the first ultraviolet absorption spectrum of the methyl radical. A strong transition observed at 216 nm was assigned to the 0 00 origin of the excitation spectrum to the 3s Rydberg state. It corresponds to the excitation of the unpaired electron of an orbital with carbon 2pz character into the 3s carbon-based orbital. However, CH3 presents a planar geometry and, as aconsequence, many one-photon transitions to the excitedstates are forbidden. The development of multiphoton spectroscopy techniques, especially resonance enhanced multiphoton ionization (REMPI), enabled the acquisition of new information on excited states5. In particular, two-photon transitions to the 3pz and 4p z Rydberg states were identified5 and have become widely used for detection of methyl radicals in the gas phase via (2+1) REMPI spectroscopy6,7.

The photodissociation dynamics of the methyl from the first electronically excited 3s Rydberg state was firstly studied by Ashfold and co-workers8 at 216.3 nm using the H-atom Rydberg tagging technique. The narrow peak observed in the measured CH2 fragment internal energy distiribution was assigned to the CH2(1 1A1) + H(2S) channel. Later, North et al.9 published a study of methyl photodissociation at 193 nm using photofragment translational spectroscopy. An anisotropy parameter β=-0.9 was determined from the measured photofragment angular distribution, consistent with the perpendicular one-photon transition 2A1’← 2A2’’ to the 3s Rydberg state. More recently, Wu et al.10,11 reported a study on the effect of the parent internal excitation in the photodissociation dynamics of the methyl radical on the 3s Rydberg state at 212.5 nm using the H-atom Rydberg tagging time-of-flight technique. However, to our knowledge, similar

experimental studies on the photodissociation of the methyl radical via the 3pz and 4pz Rydberg states have never been reported.

Westre and co-workers12,13 investigated the predissociation dynamics of the 3s Rydberg state for CH 3 and CD 3 radicals using resonance enhanced Raman spectroscopy. Subpicosecond lifetimes of around 90 fs for CH3 in the 000 band were estimated. However, it is well known that lifetimes extracted from spectral linewidths or indirect methods may have large errors due to competing experimental broadening effects which are difficult to quantify (e.g. Doppler or pressure broadening effects).

Theoretical studies on the photodissociation dynamics of methyl are very scarce13–16. Yu et al.14 performed a small basis set restricted Hartree-Fock calculation followed by configuration interaction considering both single and double substitutions (RHF-CISD) in order to obtain excitation energies for excited states and to discuss the possible fragmentation pathways, CH3 → CH2 + H and CH3 → CH + H2, for the 3s and 3p Rydberg states. Although radical dissociation of the 3pz state can thermodynamically form the 3B1, 1 1A1, 1 1B1 and 2 1A1 states of CH2 based on orbital correlations, the dominant reaction pathway was predicted to be CH2 (1 1B1) + H. In that work, a much larger reaction barrier for radical predissociation at planar geometry from the 3pz state than from the 3s state was predicted, in agreement with the higher resolution observed in the REMPI spectra via the 3pz state.

Recently, we reported an experimental and theoretical study on the femtosecond predissociation dynamics of selected vibrational states of the 3p z Rydberg state of CH3 and CD317 . In a three-color femtosecond laser experiment, methyl radicals were produced in high density from methyl iodide dissociation by a first pulse at 201.2 nm; a second laser pulse, tuneable in the region around 330 nm, was used to transfer the population from selected vibrational states of ground state methyl to the 3p z Rydberg state; finally a delayed pulse centered at 400 nm ionized the excited methyl radicals, at a controlled time delay after the excitation (≈330 nm) pulse. Subpicosecond lifetimes were measured, showing a decreasing trend as vibrational excitation in the symmetric stretch and umbrella modes was increased. High-level ab initio calculations of the electronic states involved in the process allowed us to rationalize the measured lifetimes in terms of an electronic predissociation process induced by a nonadiabatic coupling between the Rydberg state and a valence repulsive excited state. The measurements carried out did not permit, however, to extract information about the final fate of the dissociation process up to the photoproducts (CH2 + H), such as their internal energy or angular distributions, and therefore on the global photodissociation mechanism.

In the present study, we report for the first time a velocity map and slice ion imaging study on the photodissociation of the methyl radical via the 3s and 3pz Rydberg states using nanosecond pump-probe laser pulses. Fig. 1 shows a scheme of the experimental procedure used here. A molecular beam of cold methyl radicals is produced by flash pyrolysis of a precursor molecule. The methyl radicals are excited in 000 transitions either to the 3s Rydberg state at 216 nm through a one-photon process, or to the 3pz Rydberg state at 333.45 nm in a two-photon process. The produced H (2S) photofragments are detected using a (2+1) REMPI scheme at 243.1 nm. The experimental results are interpreted with the help of new highly correlated ab initio calculations performed to draw a qualitative picture of the full dissociation process involving non-adiabatic couplings and conical intersections.

The paper is organized as follows: in Section 2 the experimental and theoretical approaches are presented. In Section 3 the most relevant experimental and theoretical results are presented and discussed, and, finally, Section 4 is dedicated to present the most important conclusions of the work.

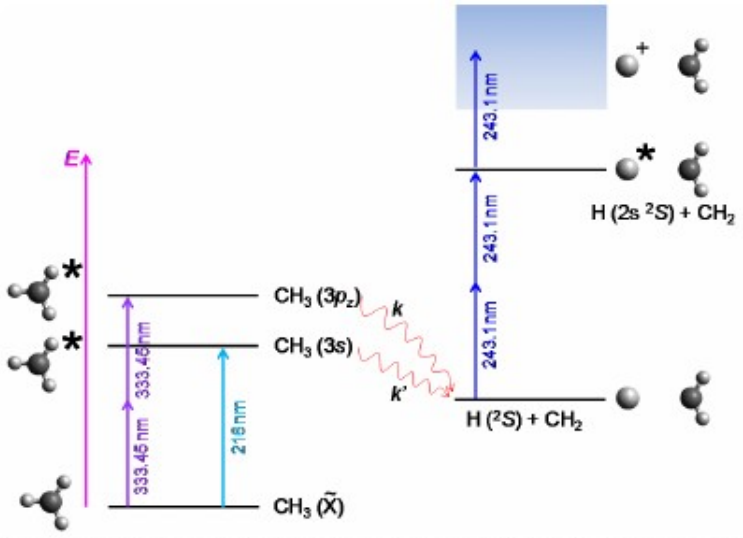

Figure 1. Scheme of the experimental procedure. A first nanosecond laser pulse centered at 333.45 nm or 216 nm is used for a two-photon $3p_z$ Rydberg state resonant excitation or a one-photon 3s Rydberg state resonant excitation, respectively. The H(²S) atom fragments following dissociation of these Rydberg states are detected using a (2+1) REMPI scheme at 243.1 nm.

Methods

Experimental

The main characteristics of the experimental setup have been described in detail previously18. The whole experiment runs at a repetition rate of 10 Hz. The cold supersonic beam of methyl radicals is generated by flash pyrolysis of di-tert-butyl peroxide (see, for instance, refs. 19 and 20]. The precursor was seeded in helium (10%, 1 atm backing pressure) and expanded into vacuum using a pulsed nozzle (General Valve Series 9, 0.5 mm orifice) with a heated SiC tube mounted at the exit19,20 .

The gas pulse passes through a skimmer (Beam Dynamics, Standard Model 2, 0.5 mm diameter orifice) and reach the ionization chamber where the molecular beam is intersected at right angles, in the middle of the electrical plates of a time-of-flight (TOF) mass spectrometer, by the excitation and the probe laser pulses, which are focused (f = 25 cm) and counter propagated to each other. A sum-frequency mixing nonlinear crystal is used to combine the fundamental and second harmonic of a Nd:YAG (Quanta Ray Pro 230) pumped dye laser (Sirah Cobra-Stretch) in order to generate the excitation radiation at 216 nm used to populate the 3s Rydberg state by one-photon (2A'1 ← 2A''2) transition. In the case of the 3pz Rydberg state, the second harmonic of this laser is used directly in order to set the wavelength at 333.45 nm, centered at the Q branch of the 3pz (2A''2 ← 2A''2) 000 transition for a two-photon process. The H atoms produced are detected 10 ns later via a (2+1) REMPI scheme at 243.1 nm corresponding to the 2s (2 S1/2) ← 1s (2S1/2) two-photon transition, using a Nd:YAG (Quanta Ray Pro 190) pumped frequency doubled dye laser (Sirah Cobra-Stretch). The probe laser frequency was scanned over the Doppler profile in the resonant transition frequency in order to ionize all photofragment velocities21.

The H+ images are recorded using our velocity map imaging (VMI) apparatus in the single-field configuration22,23 . The generated H+ ions are accelerated by an electric potential of 5 kV applied to the repeller plate and pass through a field-free TOF region (45 cm) before hitting the impedance matched microchannel plates (MCPs, Chevron configuration, 40 mm diameter). The MCPs can be gated with a high voltage pulse to allow only the ions of interest to be detected. The resulting electron avalanche strikes a phosphor screen (P47), thereby creating the ion image, which is recorded by a CCD camera (SONY 1024 x 768 pixel) controlled using National Instruments (NI) LabView 7.1 and IMAQ VISION software. The final image is obtained as the sum of around 20 000–100 000 laser shots, depending on the quality of the signal.

For the photodissociation experiments from the 3s Rydberg state, we have used delayed pulsed extraction slicing22,24. Briefly, the delayed pulsed extraction allows the ion cloud to spread in velocities so that the arrival time of the ion packet has a width of several hundreds of nanoseconds. By using a narrow detector time gate of a few tens of nanoseconds, we are able to image only the central slice of the ion packet. Since for the photodissociation experiments from the 3 pz Rydberg state, the measured H-atom translational energy spectrum does not present a better resolution using this technique, we decided to employ the regular VMI pulsed extraction in order to increase the signal-to-noise ratio.

The velocity map H+ images are quadrant symmetrised and Abel inverted using the Hankel transform, while the sliced recorded images are only quadrant symmetrised, prior to extracting the translational energy and angular distributions. Independent velocity-radius calibration of the apparatus is done by measuring resonantly ionized CH3(v=0) fragments produced after the photodissociation of CH3I at 333.45 nm (one color pump–probe experiment) at different repeller potentials, taking advantage of the well known kinetic energy release of the I(2 P 3/2) yielding channel at this photolysis wavelength18.

Theoretical

Previous ab initio calculations17 of CH3 electronic states along the dissociation path were performed preserving the C2v symmetry. In order to get insight into the eventual couplings between potential energy surfaces that may arise for planar symmetry breaking, new ab initio calculations using the Cs representation have been performed along the dissociation path optimized in our previous work17 using the MOLPRO suite of programs25. To break the equilibrium C2v symmetry, the radical was bended defining an angle of 0.010 between the plane of the CH2 fragment and the dissociative C-H coordinate, keeping only the symmetry plane perpendicular to the CH2 fragment. In this way, the energy profile of the reaction remains nearly unchanged, but the symmetry breaking mixes the A1 and B1 states in the C2v representation into A' states (Cs symmetry) that can be coupled.

As in our previous work, the aug-cc-pVTZ basis26 containing diffuse orbitals was employed for a correct description of the Rydberg states. To reproduce the several excited states involved in the process, six states of A' symmetry were computed using multi-configurational self-consistent theory (CASSCF) followed by internally contracted multi-reference configuration interaction (MRCI) method27. For this purpose, seven a' and three a'' orbitals were included in the active space, while two internal a' orbitals were kept doubly occupied in all configurations. At MRCI level, the core 1ª' orbital was frozen. Additionally, the non-adiabatic couplings matrix elements (NACME) between all the states were computed at ab initio level by finite differences of the MRCI wavefunction28.
The six adiabatic potential energy curves were then diabatized sequentially using a 2x2 diabatization model following a procedure similar to the previously described17. It must be emphasized that using this procedure, the couplings between crossing states in the constructed diabatic representation can be directly extracted.ç

Results and Discussion

Fig. 2a shows the slice image for the H(2S) atoms obtained after photodissociation of the methyl radical at 216 nm using a parallel polarization configuration of the lasers employed for photolysis and probe. The observed single ring shows perpendicular character and corresponds to the formation of the H(2S) atom in the photodissociation of the CH3 3s Rydberg state populated by a one-photon absorption at 216 nm. Angular integration of the image leads to the total translational energy distribution (TED) also shown in Fig 2a. Vertical bars represent the maximum available translational energy for the CH2(3B1) + H(2S) and CH2(1 1A1) + H (2S)channels, given by:

$$E_{av} = h\nu - E_D - E_i(\mathrm{CH_3}) \qquad (1)$$

where hν is the excitation photon energy, ED is the dissociation energy of CH3: 4.69 ± 0.05 eV 29 and 5.09 eV 30 for the ground and first excited state of CH2, respectively, and Ei is the internal energy of the methyl radical in the molecular beam.
The narrow peak observed in the TED is assigned to H(2S) atoms in correlation with the methylene radical in the first excited 1 1A1 state without significant rovibrational excitation, in agreement with the previous work by Ashfold and coworkers8. They reported an analogous CH2 photofragment internal energy spectrum in their study of the methyl radical photodissociation at 216.3 nm. The present results are also consistent with the work of Wu et al.10 at 212.5 nm.
Radial integration of the image shown in Fig. 2a yields the angular distribution depicted in Fig. 2b. The red line represents the fit to eq (2):

$$I(\theta) = \frac{\sigma}{4\pi}\left[1 + \beta P_2\left(\cos\theta\right)\right] \qquad (2)$$

where θ is the angle between the photofragment recoil velocity and the photolysis laser polarization direction, σ is the absorption cross section, β is the anisotropy parameter and P2 is the second Legendre polynomial. We have obtained a value of β = -0.85 ± 0.05 which is consistent with the perpendicular one-photon transition 2A1' ← 2A2'' to the 3s Rydberg state (in D3h group symmetry) and with a fast dissociation process. A similar anisotropic angular distribution was measured by North and coworkers9 in their study of methyl photodissociation at 193 nm using photofragment translational spectroscopy.
The velocity map image for H(2S) atoms recorded after two-photon excitation at 333.45 nm using a parallel polarization configuration of both lasers is shown in Fig. 3a. Surprisingly, no ring is observed in contrast with the image measured for the dissociation of the 3s Rydberg state (see Fig. 2a). An unstructured blot is observed as a result of the photodissociation of methyl from the 3pz Rydberg state. The corresponding total translational energy distribution obtained by angular integration of the Abel-inverted image is presented in Fig. 3b. The vertical lines represent the maximum available translational energy, obtained using eq (1), for the energetically open CH2(3B1) + H(2S), CH2(1 1A1) + H(2 S) and CH2(1 1B1) + H (2S) channels. The observed broad Boltzmann distribution indicates that the H atoms are produced in correlation with highly ro-vibrationally excited methylene fragments, which makes difficult the clear assignment of the CH2 electronic state. Such transfer between translational and internal energy of the fragments is usually associated either

with a statistical dissociation process or with a slow process characterized by an intermediate state with a long lifetime.
The Abel-inverted image was radially integrated for selected regions of about 40 pixels width, and the resulting speed- dependent angular distributions were fitted to eq (3):

$$I(\theta) = \frac{\sigma}{4\pi}\left[1 + \beta_2 P_2(\cos\theta) + \beta_4 P_4(\cos\theta)\right] \qquad (3)$$

In this case, two anisotropy parameters, β2 and β4, are used since a two-photon transition is employed to populate the 3pz Rydberg state. The limiting values for the anisotropy parameters β 2 and β4 for a two-photon transition are 2.86 and 1.14 for a parallel transition and -1.43 and 0.43 for a perpendicular transition. The fitted β2 and β4 parameters are represented as a function of the H(2S) atom fragment speed in Fig. 4. The observed values are close to zero for both parameters oscillating between ≈-0.3 and ≈0.3. Such isotropic angular distribution implies that the information related to the anisotropy of the process (including the absorption step) is lost during dissociation due to a longer reaction time than the characteristic rotational period of the molecule.

The results listed above are discordant with the previous reported lifetimes of the 3pz Rydberg state lying in the femtosecond time scale17. In order to understand the differences observed in the measured translational energy distributions of the H fragment for photodissociation of the 3s and 3pz Rydberg states of methyl and the apparent contradiction between the present results for the photodissociation of the 3pz state and the lifetimes previously measured in the femtosecond time scale17, the potential energy curves of the first six electronic states of A' symmetry (in the Cs symmetry group) along the dissociative coordinate C-H have been calculated, and are plotted in Fig. 5 in both the diabatic and adiabatic representations. Looking at the curves

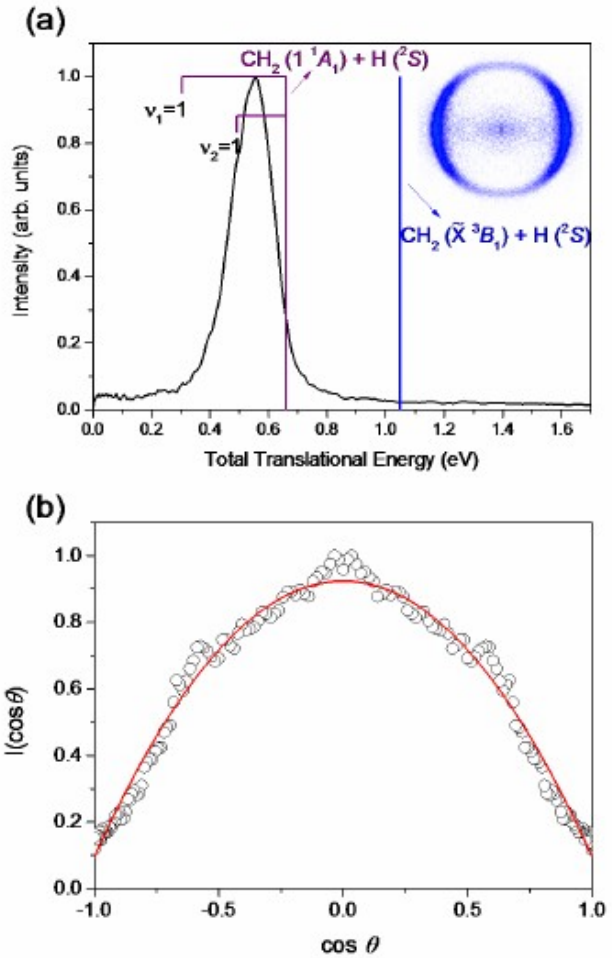

Figure 2. (a) Slice image for H(²S) atoms produced from the photodissociation of the 3*s* Rydberg state of the methyl radical by 216 nm one-photon absorption and the corresponding total translational energy distribution obtained by angular integration of the image. The contribution from the probe laser alone has been carefully subtracted. The vertical bars indicate the maximum available energy for the $CH_2(\tilde{X}\ ^3B_1) + H(^2S)$ and $CH_2(1\ ^1A_1) + H(^2S)$ channels considering experimental values from refs. 28 and 29. (b) Angular distribution obtained by radial integration of the image. Open circles: experimental points. Solid line: fit to eq (2). An anisotropy parameter of β=-0.85±0.05 is obtained.

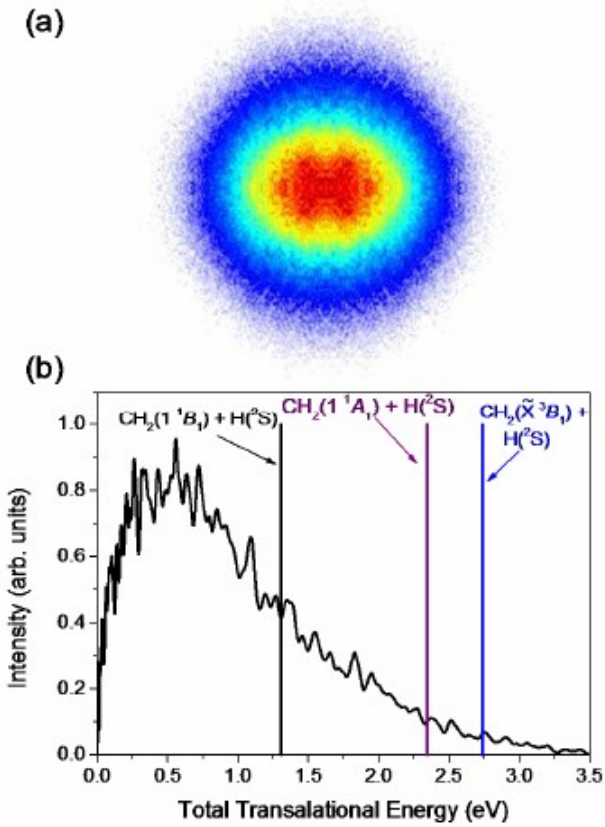

Figure 3 (a) Velocity map raw image for H(²S) atoms produced from the photodissociation of the 3p_z Rydberg state of the methyl radical by 333.45 nm two-photon absorption. The contribution from the probe laser alone has been carefully subtracted. (b) Total translational energy obtained by angular integration of the Abel inverted image shown in (a). Vertical bars indicate the maximum available energy for different $CH_2 + H(^2S)$ channels considering the experimental values from refs 28 and 29.

of the diabatic representation, we observe that the 3s Rydberg state crosses a valence state leading directly to dissociation into the CH2(1 1A1) state (denoted as valence-A1 in this work). This is a typical predissociation mechanism where only one channel is energetically open if the relaxation to the ground state is considered forbidden. In addition, the 3s Rydberg state lies at an energy comparable to that of the CH2(1 1A1) + H channel, implying that only few rovibrational states of the CH2 fragments are accessible. As a result, the photodissociation process presents a narrow energy distribution, consistent with the present experimental results (Fig. 2).

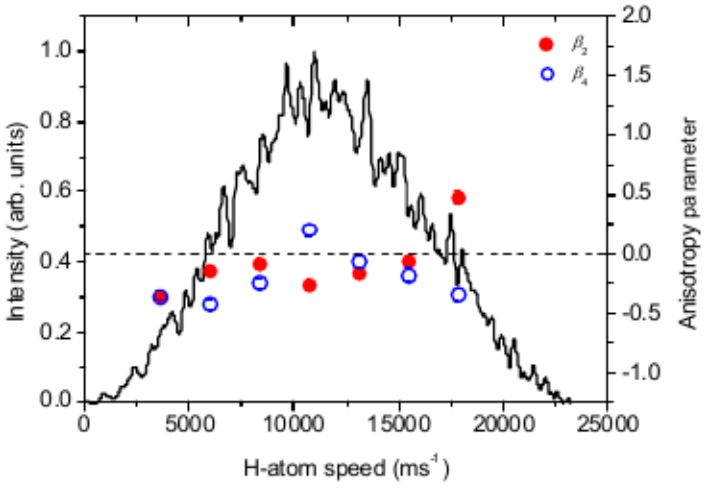

Figure 4 β_2 and β_4 anisotropy parameters characterizing the angular distribution as a function of the speed distribution of the H(^2S) atoms produced from the 3p_z Rydberg state photodissociation in CH_3.

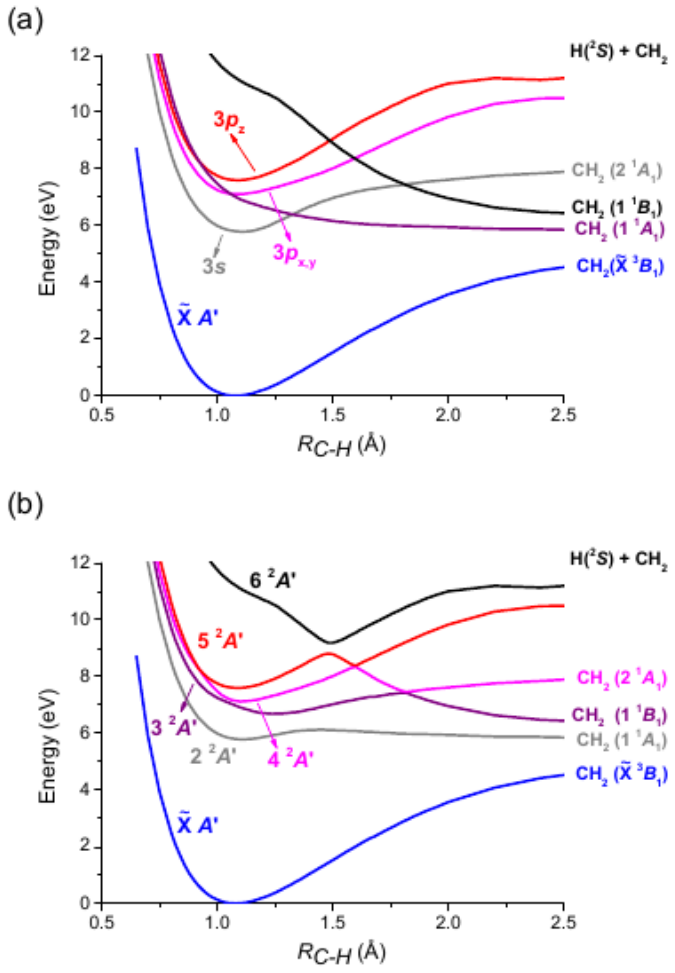

Figure 5 *Ab initio* diabatic (a) and adiabatic (b) potential energy curves of *A'* symmetry along the C–H coordinate, relevant for predissociation of the 3*s* and 3p_z Rydberg states of the methyl radical.

The results obtained for the photodissociation of the 3pz Rydberg state are, however, more surprising. Indeed, in our previous work17, subpicosecond lifetimes for the 3pz Rydberg state were reported, indicating that photodissociation is governed by a predissociation mechanism. Such result is in agreement with the potential energy curves shown in Fig. 5a where a crossing between the 3pz Rydberg state and a valence repulsive state that correlates with CH 2(1 1B1) is observed (this repulsive state is denoted valence-B1). However, significant differences are appreciable between the two 3s and 3pz Rydberg states. First, while a single electronic state of CH2 is energetically available for the 3s Rydberg state photodissociation, three electronic states are open for the Rydberg 3pz state with enough available energy to populate a wide range of rovibrational states. Furthermore, the valence- B 1 state also crosses both the 3px,y and 3s Rydberg states at larger C-H distances. As long as the system is forced to remain in the C2v symmetry, the dissociation is not affected by those crossings, because the corresponding electronic states do not couple. However, when the planar symmetry is broken, couplings between these states can arise. The adiabatic curves of Fig. 5b associated with valence-B1 and 3px,y or 3s Rydberg states are nearly degenerate around RC-H=1.6 Å or RC-H=1.8 Å, respectively, without crossing each other. This may indicate that these regions are located in the vicinity of conical intersections (CI). To confirm their existence, an automatic search for CIs was performed at the CASSCF level using MOLPRO, and indeed it was found that both points are CIs. In addition to these two CIs, a third one was found between the valence-A1 state and the 3pz Rydberg state at RC-H ≈ 1.1 Å (at CASSCF level), that at MRCI level shifts to the repulsive region. Table 1 summarizes the characteristics of the three Cis.

To get a better insight on the role of the couplings in the photodissociation dynamics, the electronic couplings associated with the diabatic representation and the kinetic (derivative) couplings associated with the adiabatic representation are plotted in Fig. 6. We should keep in mind that by construction there are no electronic couplings in the adiabatic representation and that the kinetic couplings diverge in a conical intersection. If the representation varies from adiabatic to diabatic, the kinetic couplings nearly vanish. In the present work, we have assumed that they are negligible and all couplings between states are purely electronic. As it can be seen in Fig. 6, couplings associated with CIs (dashed lines) and "permanent" couplings (solid lines), i.e. those already present in the C2v symmetry and not associated with a CI, exhibit a different behavior. The permanent couplings are broad in the adiabatic representation, leading to electronic couplings that remain strong for all distances in the diabatic representation. On the contrary, kinetic couplings near conical intersections are intense but very narrow in the adiabatic representation, leading to very small electronic couplings, three or four orders of magnitude lower than the permanent couplings, in the diabatic representation.

According to the Landau-Zenner model31,32, the diabatic transition probability is proportional to the V/ΔE ratio, where V is the potential coupling intensity and ΔE is the adiabatic potential energy difference. Permanent couplings are strong, but are associated with large ΔE values. Their efficiency will be active in a wide range, depending on the shape of the adiabatic curves and how fast ΔE varies with RC-H. The width of the kinetic coupling is usually a good indicator of the range of efficiency. For a CI, the situation is completely different. The potential couplings are small and inefficient, except in its vicinity where ΔE becomes very small, leading to a high transition probability, but in a very narrow region. This implies that the conical intersection between the valence-A1 and the 3pz states located in the repulsive part of the curves is not relevant in the present work. This CI is located at relatively high energy so that the region of efficiency cannot be accessed in the present experimental work. However, if higher rovibrational levels of the 3pz state were populated, this CI would probably reduce significantly the lifetime of

Table 1. $R_{C\text{-}H}$ and HCH angle for conical intersections found at CASSCF level.

Electronic states involved	$R_{C\text{-}H}$ (Å)	HCH angle (degrees)
3*s* Rydberg and valence-B_1	1.85	162.0
$3p_{x,y}$ Rydberg and valence-B_1	1.62	133.9
$3p_z$ Rydberg and valence-A_1	1.13	133.3

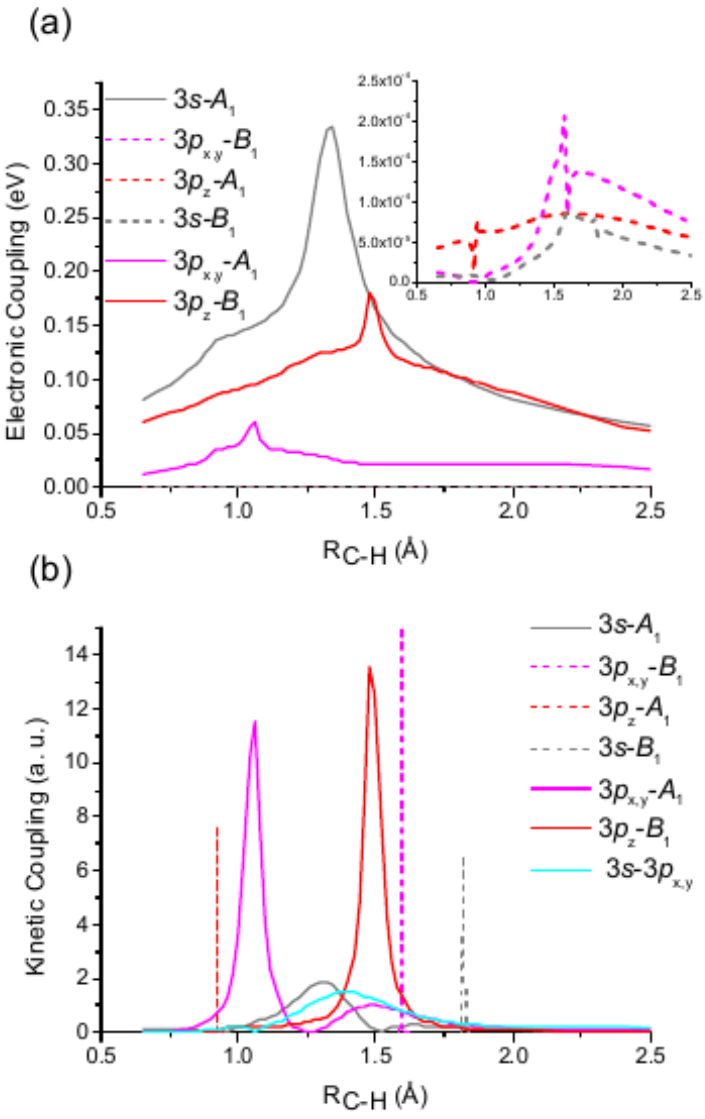

Figure 6 Electronic (a) and kinetic (b) couplings between the different *A'* states of C_s symmetry involved in the photodissociation of the 3*s* and $3p_z$ Rydberg states of methyl. The couplings associated with the C_{2v} symmetry are plotted as solid lines, while couplings arising with the C_{2v} symmetry breaking are plotted as dashed lines. For clarity, valence states are labelled according to the symmetry of the CH_2 fragment. The inset in panel (a) corresponds to an expanded view of the region between 0 and $2.5x10^{-4}$ eV of the *y*-axis.

the 3pz state since the transition at this CI will directly compete with the predissociation mechanism through the valence-B 1 CI.
A clear picture of the photodissociation mechanism can now be drawn. Firstly, a standard coupling between the 3pz Rydberg state and the valence-B1 state allows the methyl radical to predissociate. Since this coupling is quite strong, this process should be relatively fast in agreement with the subpicosecond lifetimes reported previously for this Rydberg state in the femtosecond time-resolved experiments17. After this first step, the system passes in the vicinity of two conical intersections before reaching the free photofragment region. In the first CI, the probability of a transition to the 3px,y Rydberg state is high. The predissociation of this 3px,y state can lead either directly to photoproducts formation through the valence-A1 state, or relax to the 3s Rydberg state, since the 3px,y state is coupled to the valence-A1 state, which is also coupled to the 3s Rydberg state. We note that taking into account the available energy, a transfer from translational modes into different rovibrational modes is also possible. Moreover, if the transition to the 3px,y state is not effective and the system stays in the valence-B1 state, it can also relax to the 3s state directly through the second CI. These reaction pathways accessed through the two CI are consistent with a much longer reaction time and explain the Bolztmann-type energy distribution observed in Fig. 3b for the CH 3 3pz state dissociation, in contrast to the narrow distribution observed for the 3s state, associated with a typical predissociation pathway. Similar behavior involving several conical intersections and valence-A1 and valence-B1 are expected for higher Rydberg states, as for instance the 4pz.

Conclusions

The photodissociation dynamics of the 3s and 3pz Rydberg states of the methyl radical have been studied using velocity map and slice ion imaging techniques in combination with pump-probe nanosecond laser pulses. The reported translational energy and angular distributions for the H (2S) fragments highlight a different predissociation mechanism for the two 3s and 3pz Rydberg states. High level ab initio calculations have been performed to get a deeper understanding of the photodissociation dynamics of these two Rydberg states of methyl. For the 3pz Rydberg state, after a first predissociative step, two conical intersections allow the system to relax to lower electronic states, opening reaction pathways leading to methylene photofragment in different electronic states and allowing a transfer of energy between translational and internal modes, while for the 3s Rydberg state a typical direct predissociation mechanism is recovered.

Acknowledgements

We thank Prof. Domenico Stranges for his help in setting up the flash pyrolysis oven in our molecular beam machine. S.M.P. acknowledges financial support from Campus de Excelencia Internacional Moncloa and LASING S.A. D.V.C. acknowledges a contract from MINECO under the Fondo de Garantía Juvenil. A.Z. thanks the support from the European Research Council under the European Union’s 7th Framework Program (FP7/2007-2013)/ERC Grant agreement 610256 (NANOCOSMOS). M.G.G. is grateful to Spanish MINECO for a contract through Programa de Técnicos de Apoyo a Infraestructuras. This work has been financed by the Spanish MINECO (grants FIS2011-29596-C02-01, CTQ2012-37404-C02-01, FIS2013-40626-P and CTQ2015-65033-P) and by COST Actions CM1401 and CM05. This research has been carried out within the Unidad Asociada Química Física Molecular between Departamento de Química Física of Universidad Complutense de Madrid (UCM) and Consejo Superior de Investigaciones Científicas (CSIC). The facilities provided by the Centro de Láseres Ultrarrápidos at UCM are acknowledged. The Centro de Supercomputación de Galicia (CESGA, Spain) and CTI (CSIC) are acknowledged for the use of their resources.

References

1 R. P. Wayne, Chemistry of Atmospheres, Oxford University Press, Oxford, 2000.
2 H. Feuchtgruber, F. P. Helmich, E. F. van Dishoeck and C. M. Wright, Astrophys. J. Lett., 2000, 535, L111.
3 K. C. Smyth and P. H. Taylor, Chem. Phys. Lett., 1985, 122, 518–522.
4 G. Herzberg and J. Shoosmith, Can. J. Phys., 1956, 34, 523.
5 J. W. Hudgens, T. G. DiGiuseppe and M. C. Lin, J. Chem. Phys., 1983, 79, 571–582.
6 J. M. Jasinski, B. S. Meyerson and B. A. Scott, Annu. Rev. Phys.Chem., 1987, 38, 109–140.

7 W. Zhang, H. Kawamata, A. J. Merer and K. Liu, J. Phys. Chem. A, 2009, 113, 13133–13138.
8 S. H. S. Wilson, J. D. Howe, K. N. Rosser, M. N. R. Ashfold and R. N.Dixon, Chem. Phys. Lett., 1994, 227, 456–460.
9 S. W. North, D. A. Blank, P. M. Chu and Y. T. Lee, J. Chem. Phys., 1995, 102, 792–798.
10 G. Wu, B. Jiang, Q. Ran, J. Zhang, S. A. Harich and X. Yang, J. Chem. Phys., 2004, 120, 2193–2198.
11 G. Wu, J. Zhang, S. A. Harich and X. Yang, Chin. J. Chem. Phys., 2006, 19, 109–116.
12 S. G. Westre, P. B. Kelly, Y. P. Zhang and L. D. Ziegler, J. Chem. Phys., 1991, 94, 270–276.
13 S. G. Westre, T. E. Gansberg, P. B. Kelly and L. D. Ziegler, J. Phys. Chem., 1992, 96, 3610–3615.
14 H. T. Yu, A. Sevin, E. Kassab and E. M. Evleth, J. Chem. Phys., 1984, 80, 2049–2059.
15 P. Botschwina, E. Schick and M. Horn, J. Chem. Phys., 1993, 98, 9215–9217.
16 A. M. Mebel and S.-H. Lin, Chem. Phys., 1997, 215, 329–341.
17 G. Balerdi, J. Woodhouse, A. Zanchet, R. de Nalda, M. L. Senent, A. García-Vela and L. Bañares, Phys. Chem. Chem. Phys., 2016, 18, 110–118.
18 L. Rubio-Lago, A. García-Vela, A. Arregui, G. A. Amaral and L. Bañares, J. Chem. Phys., 2009, 131, 174309.
19 D. W. Kohn, H. Clauberg and P. Chen, Rev. Sci. Instrum., 1992, 63, 4003–4005.
20 D. Stranges, M. Stemmler, X. Yang, J. D. Chesko, A. G. Suits and Y. T. Lee, J. Chem. Phys., 1998, 109, 5372–5382.
21 R. L. Toomes, P. C. Samartzis, T. P. Rakitzis and T. N. Kitsopoulos, Chem. Phys., 2004, 301, 209–212.
22 V. Papadakis and T. N. Kitsopoulos, Rev. Sci. Instrum., 2006, 77, 083101.
23 L. Rubio-Lago, G. A. Amaral, A. N. Oldani, J. D. Rodríguez, M. G. González, G. A. Pino and L. Bañares, Phys. Chem. Chem. Phys., 2010, 13, 1082–1091.
24 C. R. Gebhardt, T. P. Rakitzis, P. C. Samartzis, V. Ladopoulos and T. N. Kitsopoulos, Rev. Sci. Instrum., 2001, 72, 3848–3853.
25 H.-J. Werner, P. J. Knowles, G. Knizia, F. R. Manby, M. Schütz, P. Celani, T. Korona, R. Lindh, A. Mitrushenkov, G. Rauhut, K. R. Shamasundar, T. B. Adler, R. D. Amos, A. Bernhardsson, A. Berning, D. L. Cooper, M. J. O. Deegan, A. J. Dobbyn, F. Eckert, E. Goll, C. Hampel, A. Hesselmann, G. Hetzer, T. Hrenar, G. Jansen, C. Köppl, Y. Liu, A. W. Lloyd, R. A. Mata, A. J. May, S. J. McNicholas, W. Meyer, M. E. Mura, A. Nicklass, D. P. O'Neill, P. Palmieri, D. Peng, K. Pflüger, R. Pitzer, M. Reiher, T. Shiozaki, H. Stoll, A. J. Stone, R. Tarroni, T. Thorsteinsson and M. Wang, MOLPRO, version 2009.1, a package of ab initio programs, 2003.
26 R. A. Kendall, T. H. Dunning Jr and R. J. Harrison, J. Chem. Phys., 1992, 96, 6796.
27 H.-J. Werner and P. J. Knowles, J Chem Phys, 1988, 89, 5803–5814.
28 H.-J. Werner, B. Follmeg and M. H. Alexander, J. Chem. Phys.,1988, 89, 3139–3151.